

Emergent topological superconductivity in skyrmion magnet/d-wave superconductor heterostructures

Zhi-Jian Li(李志坚) and Qiang Han(韩强)

Citation: Chin. Phys. B, 2026, 35 (**6**): 067403. DOI: 10.1088/1674-1056/ae4c6e
http://cpb.iphy.ac.cn; http://iopscience.iop.org/cpb

What follows is a list of articles you may be interested in

Strongly tunable Ising superconductivity in van der Waals $NbSe_{2-x}Te_x$ nanosheets

Jingyuan Qu(曲静远), Guojing Hu(胡国静), Cuili Xiang(向翠丽), Hui Guo(郭辉), Senhao Lv(吕森浩), Yechao Han(韩烨超), Guoyu Xian(冼国裕), Qi Qi(齐琦), Zhen Zhao(赵振), Ke Zhu(祝轲), Xiao Lin(林晓), Lihong Bao(鲍丽宏), Yongjin Zou(邹勇进), Lixian Sun(孙立贤), Haitao Yang(杨海涛), and Hong-Jun Gao(高鸿钧)
Chin. Phys. B, 2025, 34 (**6**): 067401. DOI: 10.1088/1674-1056/adc7f4

Majorana zero modes induced by skyrmion lattice

Dong-Yang Jing(靖东洋), Huan-Yu Wang(王寰宇), Wen-Xiang Guo(郭文祥), and Wu-Ming Liu(刘伍明)
Chin. Phys. B, 2023, 32 (**1**): 017401. DOI: 10.1088/1674-1056/ac6ee7

Evidence for topological superconductivity: Topological edge states in Bi_2Te_3/FeTe heterostructure

Bin Guo(郭斌), Kai-Ge Shi(师凯歌), Hai-Lang Qin(秦海浪), Liang Zhou(周良), Wei-Qiang Chen(陈伟强), Fei Ye(叶飞), Jia-Wei Mei(梅佳伟), Hong-Tao He(何洪涛), Tian-Luo Pan(潘天洛), Gan Wang(王干)
Chin. Phys. B, 2020, 29 (**9**): 097403. DOI: 10.1088/1674-1056/abaf9c

A simple tight-binding approach to topological superconductivity in monolayer MoS_2

H Simchi
Chin. Phys. B, 2020, 29 (**2**): 027401. DOI: 10.1088/1674-1056/ab6552

Topological superconductivity in a $Bi_2Te_3/NbSe_2$ heterostructure: A review

Hao Zheng(郑浩), Jin-Feng Jia(贾金锋)
Chin. Phys. B, 2019, 28 (**6**): 067403. DOI: 10.1088/1674-1056/28/6/067403

SPECIAL TOPIC — Two-dimensional superconductivity

Emergent topological superconductivity in skyrmion magnet/d-wave superconductor heterostructures

Zhi-Jian Li(李志坚) and Qiang Han(韩强)†

Department of Physics, Renmin University of China, Beijing 100872, *China*

(Received 5 January 2026; revised manuscript received 14 February 2026; accepted manuscript online 3 March 2026)

The interplay of superconductivity with non-trivial magnetic textures is a promising route toward the engineering of topological superconductivity and Majorana quasiparticles. In this paper, we demonstrate the realization of topological superconductivity in a d-wave superconductor coupled to a skyrmion lattice. Transitions between different topological phases can be induced by tuning the chemical potential and the magnetic exchange coupling. For intermediate-coupling strength, we unveil the formation of Chern bands of conduction electrons coupled to the magnetic skyrmions and present the emergence of an effective chiral p-wave pairing induced in the non-trivial Chern band. Majorana zero modes localized at the cores of the superconducting vortex lattice are revealed for topological superconducting phases with odd superconducting Chern numbers.

Keywords: topological superconductivity, skyrmion lattice, Majorana zero modes

PACS: 74.45.+c, 75.70.Kw, 74.20.Rp

DOI: 10.1088/1674-1056/ae4c6e **CSTR:** 32038.14.CPB.ae4c6e

1. Introduction

The realization of topological superconductivity (TSC) is of fundamental importance, not only for probing exotic quantum phenomena but also for its potential application in fault-tolerant quantum computing[1,2] which relies on the non-Abelian braiding statistics of Majorana zero modes (MZMs) hosted in such systems. Inspired by Fu and Kane's[3] seminal proposal, numerous platforms have been explored to engineer TSC and MZMs based on proximity-coupled hybrid structures which combine conventional s-wave superconductors with diverse systems, ranging from topological insulators,[4–7] semiconductors with strong spin–orbit coupling (SOC),[8–12] quantum anomalous Hall insulators,[13–18] to magnetic adatom arrays.[19–24] In these setups, the emergence of TSC is governed by the interplay of the superconducting pairing correlation, the spin-degeneracy lifting, and the spin–momentum locking, which typically demands a strong SOC and sufficiently large Zeeman splitting field.

In parallel to these extensively studied systems, recent studies[25–34] have demonstrated that the non-collinear magnetic textures coupled to conduction electrons can induce a synthetic SOC and a Zeeman-like field,[20,35] which, combined with s-wave superconductivity, can lead to the formation of TSC. In particular, the skyrmion lattice (SkL),[35–40] as a topologically non-trivial magnetic texture, exerts an emergent magnetic field on conduction electrons coupled to it. This inhomogeneous magnetic field, quantized to one flux quantum h/e per skyrmion, is reported to give rise to the topological Hall effect.[41,42] Theoretical studies further predict the realization of the quantized topological Hall effect in 2D electron systems coupled to the SkL.[43–48]

Motivated by the fascinating topology nature of magnetic skyrmions, we investigate the realization of TSC in a heterostructure combining the SkL with a d-wave superconductor (dSC). Different from prior researches,[25,30] we demonstrate that the emergent gauge field generated by the skyrmion texture effectively reconstructs the normal-state bands, endowing them with non-zero Chern numbers. Upon inducing superconductivity from the superconducting substrate, the TSC phases emerge from the non-trivial Chern bands, hosting chiral Majorana edge modes along the open boundaries of a ribbon and MZMs within the vortex cores in the superconducting vortex-lattice state. Remarkably, we find that the vortex MZMs are energetically well-separated from the trivial Caroli-de Gennes–Matricon (CdGM)[49] states, conferring enhanced robustness to these topological modes.

2. Model and formalism

The system is a two-dimensional heterostructure composed of a SkL placed on top of a d-wave superconductor. The model Hamiltonian, built on the tight-binding formalism, is written as

$$\hat{H} = \sum_{\boldsymbol{r},\boldsymbol{r}',s} (-t_{\boldsymbol{r},\boldsymbol{r}'} - \mu\delta_{\boldsymbol{r},\boldsymbol{r}'}) c^{\dagger}_{\boldsymbol{r},s} c_{\boldsymbol{r}',s} + J \sum_{\boldsymbol{r},s,s'} \boldsymbol{m}(\boldsymbol{r}) \cdot \boldsymbol{\sigma}_{s,s'} c^{\dagger}_{\boldsymbol{r},s} c_{\boldsymbol{r},s'}$$

†Corresponding author. E-mail: hanqiang@ruc.edu.cn

© 2026 Chinese Physical Society and IOP Publishing Ltd. All rights, including for text and data mining, AI training, and similar technologies, are reserved.

$$+\sum_{\boldsymbol{r},\boldsymbol{r}'}\left(\Delta_{\boldsymbol{r},\boldsymbol{r}'}c^{\dagger}_{\boldsymbol{r}\uparrow}c^{\dagger}_{\boldsymbol{r}'\downarrow}+\text{H.c.}\right). \tag{1}$$

Here, $\boldsymbol{r}=m\boldsymbol{e}_x+n\boldsymbol{e}_y$ is the position vector of the lattice site, where $\boldsymbol{e}_x$ and $\boldsymbol{e}_y$ are primitive vectors (the lattice constant is chosen as the length unit) and m,n are integers. The spin index s takes values $\uparrow,\downarrow$. The chemical potential is denoted by μ. The hopping amplitude $t_{\boldsymbol{r},\boldsymbol{r}'}=t$ or t' for hopping between nearest or next-nearest neighbors, respectively. The spin-singlet superconducting pairing amplitude are represented by $\Delta_{\boldsymbol{r},\boldsymbol{r}'}$. In this paper, we focus on the d-wave pairing which has been used in TI-based hybrid systems to realize first order[50,51] and second-order[52,53] TSC. The pairing potential $\Delta_{\boldsymbol{r},\boldsymbol{r}\pm\boldsymbol{e}_x}=-\Delta_{\boldsymbol{r},\boldsymbol{r}\pm\boldsymbol{e}_y}=\Delta_0$, where Δ_0 is the d-wave order parameter.

The magnetic exchange interaction between the electrons and the magnetic SkL is described by the J term in Eq. (1). Here, the magnetic texture, corresponding to a double-$\boldsymbol{Q}$ SkL,[38,40] is represented by

$$\begin{aligned}\boldsymbol{m}(\boldsymbol{r}) &= [\sin(\boldsymbol{Q}_1\cdot\boldsymbol{r})\boldsymbol{e}_1+\sin(\boldsymbol{Q}_2\cdot\boldsymbol{r})\boldsymbol{e}_2\\ &\quad+[m_0+\cos(\boldsymbol{Q}_1\cdot\boldsymbol{r})+\cos(\boldsymbol{Q}_2\cdot\boldsymbol{r})]\hat{\boldsymbol{z}}]/N_{\boldsymbol{r}},\end{aligned} \tag{2}$$

where $\boldsymbol{Q}_i=\frac{2\pi}{\lambda}\boldsymbol{e}_i$ represents the wave vectors of two spin spirals, with $\boldsymbol{e}_i$ unit vectors indicating the spiral directions and λ the wavelength. $N_{\boldsymbol{r}}$ is the local normalization factor. The winding number of the SkL is defined as

$$N_{\text{sk}}=(4\pi)^{-1}\int\boldsymbol{m}(\boldsymbol{r})\cdot(\partial_x\boldsymbol{m}(\boldsymbol{r})\times\partial_y\boldsymbol{m}(\boldsymbol{r}))\,\mathrm{d}x\mathrm{d}y, \tag{3}$$

where the integral is taken over the SkL unit cell. The skyrmion number $N_{\text{sk}}=1$ for $-2<m_0<0$, and $N_{\text{sk}}=-1$ for $0<m_0<2$.

The system Hamiltonian can be re-expressed as

$$\hat{H}=\frac{1}{2}\Psi^{\dagger}H_{\text{BdG}}\Psi+\text{const.}, \tag{4}$$

where $\Psi^{\dagger}=(\Psi^{\dagger}_{\uparrow},\Psi^{\dagger}_{\downarrow},\Psi^{\text{T}}_{\uparrow},\Psi^{\text{T}}_{\downarrow})$ denotes the Nambu basis. Here, $\Psi^{\dagger}_s$ with $s=\uparrow,\downarrow$ is a row operator written as $\Psi^{\dagger}_s=(\cdots,c^{\dagger}_{\boldsymbol{r},s},\cdots)$, while $\Psi_s=(\cdots,c_{\boldsymbol{r},s},\cdots)^{\text{T}}$ is a column operator. The BdG Hamiltonian H_{BdG} is written as

$$H_{\text{BdG}}=\begin{pmatrix}H_0-\mu & \mathrm{i}\sigma_y H_\Delta\\ -\mathrm{i}\sigma_y H^{\dagger}_\Delta & -H^{*}_0+\mu\end{pmatrix}, \tag{5}$$

where the matrix element of the pairing matrix H_Δ is related to the pairing potential by $(H_\Delta)_{\boldsymbol{r},\boldsymbol{r}'}=\Delta_{\boldsymbol{r},\boldsymbol{r}'}$. The normal-state Hamiltonian is denoted by H_0, which is expressed as

$$H_0=\sigma_0 H_t+J\boldsymbol{\sigma}\cdot\boldsymbol{M}, \tag{6}$$

where the matrix element of the hopping Hamiltonian H_t is $(H_t)_{\boldsymbol{r},\boldsymbol{r}'}=t_{\boldsymbol{r},\boldsymbol{r}'}$, and $\boldsymbol{M}$ encodes the magnetic texture, whose elements are $\boldsymbol{M}_{\boldsymbol{r},\boldsymbol{r}'}=\boldsymbol{m}(\boldsymbol{r})\delta_{\boldsymbol{r},\boldsymbol{r}'}$.

3. Topological phase diagram

In this paper, we construct the double-$\boldsymbol{Q}$ SkL according to Eq. (2) by setting the spiral propagation directions $\boldsymbol{e}_{1,2}=(\pm\boldsymbol{e}_x+\boldsymbol{e}_y)/\sqrt{2}$ and an atomic-scale[38,40] SkL wavelength $\lambda=2\sqrt{2}$. The choice of $m_0=1$ gives rise to a skyrmion number $N_{\text{sk}}=-1$. Since this SkL imposes a commensurate periodic modulation on the underlying lattice, the real-space BdG Hamiltonian (5) can be Fourier transformed into the Bloch–BdG Hamiltonian $H_{\text{BdG}}(\boldsymbol{k})$, where $\boldsymbol{k}$ is the momentum in the SkL Brillouin zone. For each $\boldsymbol{k}$, the BdG equation is

$$H_{\text{BdG}}(\boldsymbol{k})|\phi_n(\boldsymbol{k})\rangle=E_n(\boldsymbol{k})|\phi_n(\boldsymbol{k})\rangle, \tag{7}$$

where $E_n(\boldsymbol{k})$ denotes the BdG energy band with $|\phi_n(\boldsymbol{k})\rangle$ the corresponding eigenvector. The bulk gap Δ_{gap} of this hybrid system is determined from the minimum of $|E_n(\boldsymbol{k})|$. The BdG Hamiltonian has particle-hole symmetry $\mathcal{C}H_{\text{BdG}}(\boldsymbol{k})\mathcal{C}^{-1}=-H_{\text{BdG}}(-\boldsymbol{k})$ with $\mathcal{C}=\tau_x K$. Thus, the system belongs to the topological class D and is characterized by the Chern number defined as[54]

$$C=\frac{1}{2\pi\mathrm{i}}\int\text{Tr}\{P(\boldsymbol{k})[\partial_{k_x}P(\boldsymbol{k}),\partial_{k_y}P(\boldsymbol{k})]\}\,\mathrm{d}^2\boldsymbol{k}, \tag{8}$$

where $P(\boldsymbol{k})=\sum_{E_n(\boldsymbol{k})<0}|\phi_n(\boldsymbol{k})\rangle\langle\phi_n(\boldsymbol{k})|$ is the projector onto the occupied BdG bands and the integral is over the SkL Brillouin zone (BZ).

In Fig. 1(a), we illustrate the topological phase diagram manifested by the variation of Δ_{gap} as a function of μ and J. A rich phase structure is exhibited. These phases, characterized by quantized superconducting Chern numbers C_{BdG}, are distinctly separated by phase boundaries where the bulk energy gap closes. Note that only Chern numbers for topological regimes with notable gaps are shown in Fig. 1(a). To probe the evolution of the topological properties, we examine the changes of Δ_{gap} and C_{BdG} with μ for fixed $J/t=3.0$, as well as with J for fixed $\mu/t=-0.7$. The results, presented in Figs. 1(b) and 1(c), reveal that the Chern number remains quantized and constant whenever the bulk gap stays open, and it changes discontinuously across certain critical parameters where the gap closes, signaling a topological phase transition.

The variation of the superconducting Chern number as a function of μ can be understood by examining the normal-state band structure. The SkL acts as a magnetic superlattice imposed on the underlying lattice, causing the reconstruction of the tight-binding electron band. To elucidate this, we choose an intermediate-coupling strength with $J/t=3$ and solve the Schrödinger equation in momentum space

$$H_0(\boldsymbol{k})|u_n(\boldsymbol{k})\rangle=\varepsilon_n(\boldsymbol{k})|u_n(\boldsymbol{k})\rangle, \tag{9}$$

where $H_0(\boldsymbol{k})$ denotes the normal-state Bloch Hamiltonian obtained from Eq. (6). Since the SkL unit-cell size is λ, there are totally $2\lambda^2=16$ bands, as shown in the inset of Fig. 2(a).

The eighth and ninth bands counted from the lowest band are well separated from their neighbors, whereas the remaining multiplets of bands exhibit significant crossings and degeneracies. The normal-state Chern number is calculated using Eq. (8). For a single-band normal-state Chern number C_n, the projector is $P(\boldsymbol{k}) = |u_n(\boldsymbol{k})\rangle\langle u_n(\boldsymbol{k})|$, where n denotes the band index. For a multi-band normal-state Chern number $C_{n_1\sim n_2}$, $P(\boldsymbol{k}) = \sum_{n=n_1}^{n_2} |u_n(\boldsymbol{k})\rangle\langle u_n(\boldsymbol{k})|$ where n_1 and n_2 are indices of the bottom and top bands of the multiplet, respectively. The results are shown in Fig. 2(a). When the Fermi level lies within the energy gap between the bottom of the eighth band and the top of the seventh band, indicated by the light green region in Fig. 2(a), the normal state is a quantized topological Hall insulator characterized by a Chern number of the occupied bands, $C_{1\sim7} = -1$. Thus, in the presence of the d-wave pairing, we get a TSC with an even Chern number[13] $C_{\rm BdG} = C_{1\sim7} - (C_8 + C_9 + C_{10\sim16}) = 2C_{1\sim7} = -2$, corresponding to the topological region $-1.4 < \mu/t < -1$. as shown in Fig. 1(b). Similarly, for $-0.24 < \mu/t < 1.0$, corresponding to the light blue region of Fig. 2(a), we have a topologically trivial phase with $C_{\rm BdG} = 2(C_{1\sim7} + C_8) = 0$.

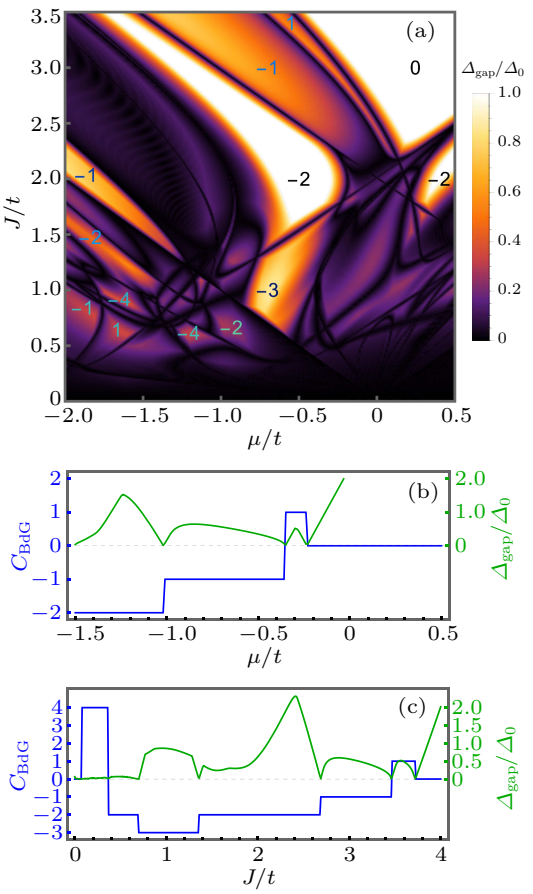


Fig. 1. (a) Topological phase diagram of the SkL-dSC model. The density plot depicts the excitation gap as a function of μ and J, and the integers in different topological regions show the associated Chern numbers. Excitation gaps (green lines) and Chern numbers (blue lines) as functions of μ with fixed $J/t = 3.0$ (b), and as functions of J with fixed $\mu/t = -0.7$ (c). The remaining parameters are $t'/t = -0.3$ and $\Delta_0/t = 0.1$.

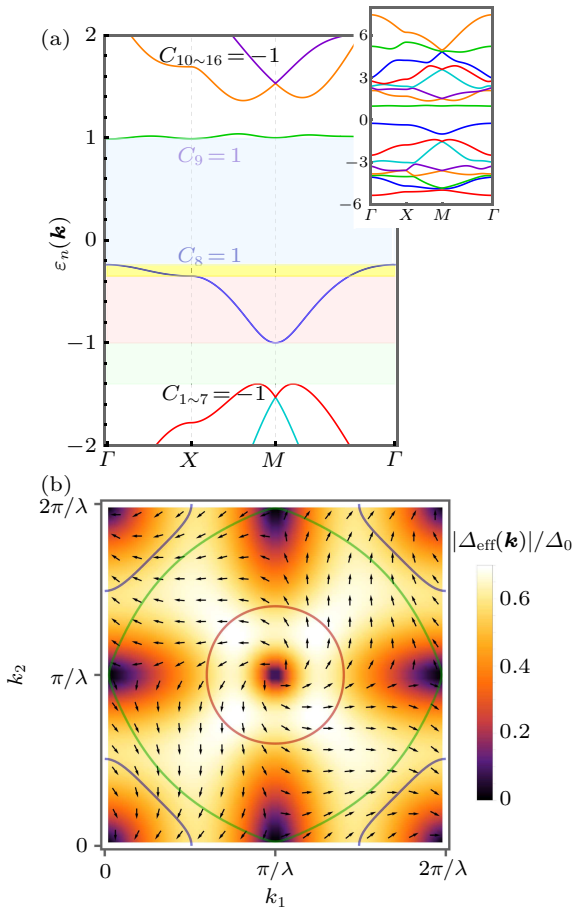


Fig. 2. (a) Band structure of the normal-state electrons. The blue and green curves show the energy dispersions of the eighth and ninth bands in the first SkL BZ, respectively. C_8 and C_9 are the corresponding Chern numbers. $C_{1\sim7}$ and $C_{10\sim16}$ denote the multi-band Chern numbers. The parameters are $t'/t = -0.3$, $J/t = 3.0$. The TRIM in the SkL BZ are $\Gamma = (0,0)$, $X = (\pi/\lambda, 0)$ and $M = (\pi/\lambda, \pi/\lambda)$. The inset displays the band structure of all the sixteen bands. (b) Momentum structure of the effective gap function $\Delta_{\rm eff}(\boldsymbol{k})$. The density plot shows the magnitude, while the arrows represent the phases of $\Delta_{\rm eff}(\boldsymbol{k})$. The red, green and blue curves are the Fermi surfaces corresponding to $\mu/t = -0.7$ (in the pink region of (a)), -0.35 (Fermi level crossing the 8-th band at X) and -0.3 (in the yellow region of (a)), respectively.

On the other hand, when the Fermi level resides in the eighth band, as shown in the pink and yellow regions of Fig. 2(a) with $-1.0 < \mu/t < -0.24$, the normal state becomes a topological Hall metal. Upon introducing d-wave pairing, we project the BdG Hamiltonian onto the eighth band since it is well separated from other bands and obtain a single-band effective pairing Hamiltonian

$$H^{\rm eff}_{\rm BdG}(\boldsymbol{k}) = \begin{pmatrix} \varepsilon_8(\boldsymbol{k}) - \mu & \Delta_{\rm eff}(\boldsymbol{k}) \\ \Delta^*_{\rm eff}(\boldsymbol{k}) & -\varepsilon_8(-\boldsymbol{k}) + \mu \end{pmatrix}, \tag{10}$$

where $\varepsilon_8(\boldsymbol{k})$ is the energy dispersion of the eighth Chern band. The effective gap function is $\Delta_{\rm eff}(\boldsymbol{k}) = \langle u_8(\boldsymbol{k})|H_\Delta(\boldsymbol{k})|u^*_8(-\boldsymbol{k})\rangle$. The quasiparticle excitation energy is $E_{\boldsymbol{k}} = \sqrt{(\varepsilon_8(\boldsymbol{k}) - \mu)^2 + |\Delta_{\rm eff}(\boldsymbol{k})|^2}$. The momentum structure of $\Delta_{\rm eff}(\boldsymbol{k})$ is illustrated in Fig. 2(b). We observe that the effective superconducting gap function vanishes at the time-reversal invariant momenta (TRIM) $\Gamma = (0,0)$, $X = (\pi/\lambda, 0)$, $Y = (0, \pi/\lambda)$, and $M = (\pi/\lambda, \pi/\lambda)$ in the SkL BZ. Both the

nodal behavior and the phase structure, as shown in Fig. 2(b), reflect the chiral p-wave pairing character given by $\Delta_{\rm eff}(\boldsymbol{k}) \propto \sin(k_1\lambda) + \mathrm{i}\sin(k_2\lambda)$. When the Fermi level crosses the energy band at the TRIM, the bulk gap vanishes and a topological phase transition occurs. Therefore, the phase boundaries, separating successive topological phases with superconducting Chern numbers -2, -1, 1, and 0, are $\mu/t = -1.0$, -0.35, and -0.24, respectively, consistent with the results shown in Fig. 1(b).

4. Chiral edge modes and Majorana vortex zero modes

While the previous section focused on the bulk properties under periodic boundary conditions, we next consider a ribbon geometry with open boundaries to explore the emergence of topologically protected boundary states. The ribbon is periodic along $\boldsymbol{e}_1$ and has two open edges along $\boldsymbol{e}_2$, as shown in Fig. 3(a). By performing a Fourier transform along the $\boldsymbol{e}_1$ direction, the energy spectra are computed and shown in Figs. 3(b)–3(d) for three distinct TSC phases. Our results unambiguously demonstrate the presence of gapless chiral edge modes (CEMs) within the bulk energy gap. The TSC phases with superconducting Chern numbers $C_{\rm BdG} = -1, -2$ and -3 host $|C_{\rm BdG}|$ pairs of CEMs, with half of them localized at each of the two opposite edges of the ribbon, in compliance with the bulk–boundary correspondence. These CEMs traverse the superconducting gap and disperse linearly near the Fermi level as a function of k_1.

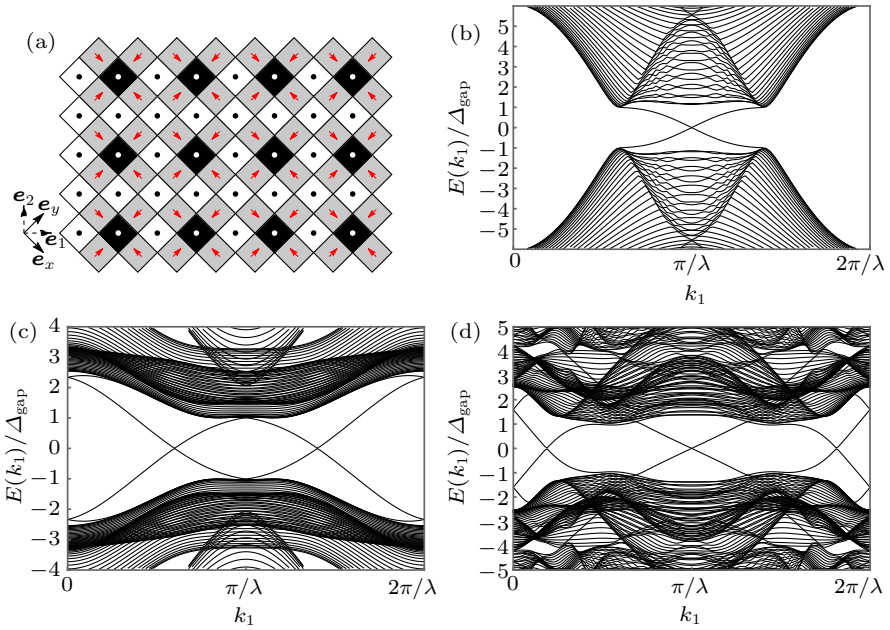


Fig. 3. (a) Distribution of the magnetic SkL on a ribbon which is periodic along the $\boldsymbol{e}_1$ direction, while open along the $\boldsymbol{e}_2$ direction. The z component of the magnetic moment is represented by the color of the square. For white (black) squares with central black (white) dot $m_z = 1$ (-1), and for gray squares with central arrow $m_z = 1/\sqrt{3}$. The red arrows denote the directions of the magnetic moments in the xy plane. (b)–(d) Energy spectra of the BdG bands for the ribbon. The exchange couplings are $J/t = 3.0$, 2.4 and 1.0, respectively. The associated superconducting Chern numbers are $C_{\rm BdG} = -1$, -2 and -3, respectively. The other parameters are $t'/t = -0.3$, $\mu/t = -0.7$, and $\Delta_0/t = 0.1$.

We now turn our attention to whether such a SkL-dSC heterostructure can host MZMs in the cores of superconducting vortices. Qualitatively similar results are observed for odd superconducting Chern numbers; therefore, we focus our discussion on the representative case of $C_{\rm BdG} = -1$. When a magnetic field $B_z(\boldsymbol{r})$ is applied normal to the 2D heterostructure, the electron hopping between sites $\boldsymbol{r}$ and $\boldsymbol{r}'$ acquires a Peierls phase factor $\exp[\mathrm{i}\frac{e}{\hbar}\int_{\boldsymbol{r}}^{\boldsymbol{r}'} \boldsymbol{A}(\boldsymbol{l})\cdot \mathrm{d}\boldsymbol{l}]$ resulting from the magnetic vector potential $\boldsymbol{A}$. For a sufficiently large magnetic field, a square vortex lattice[55] is formed. We construct the d-wave order parameter (dOP), $\Delta_{\rm d}(\boldsymbol{r}) = |\Delta_{\rm d}(\boldsymbol{r})|\,\mathrm{e}^{\mathrm{i}\theta(\boldsymbol{r})}$ in the vortex-lattice state by employing Abrikosov's solution:

$$f(x,y) = \mathrm{e}^{\mathrm{i}2\pi\tilde{y}^2} \sum_{n=-\infty}^{\infty} \mathrm{e}^{-\frac{\pi}{2}[(2\tilde{x}-n)^2 + \mathrm{i}(2\tilde{y}-n)^2]}, \tag{11}$$

where $\tilde{x} = x/L$, $\tilde{y} = y/L$ with L the size of the magnetic unit cell (MUC). Considering that $f(x,y)$ has a large core size comparable to L, we modify it by shrinking its core size according to

$$|\Delta_{\rm d}(\boldsymbol{r})| = \Delta_0 \tanh[\alpha|f(\boldsymbol{r})|], \tag{12}$$

while preserving the phase $\theta(\boldsymbol{r}) = \arg[f(\boldsymbol{r})]$. In Eq. (12), α is used to tune the vortex-core size. The magnitude and phase of the dOP in one MUC are shown in the upper-left panel of Fig. 4. Two vortices can be clearly seen. The d-wave pairing potential in Eq. (1) is then determined according to $\Delta_{\boldsymbol{r},\boldsymbol{r}+\boldsymbol{e}_{x,y}} = \pm[\Delta_{\rm d}(\boldsymbol{r}) + \Delta_{\rm d}(\boldsymbol{r}+\boldsymbol{e}_{x,y})]/2$. Note that the pairing potential is not determined self-consistently because this has no impact on the overall topological features.

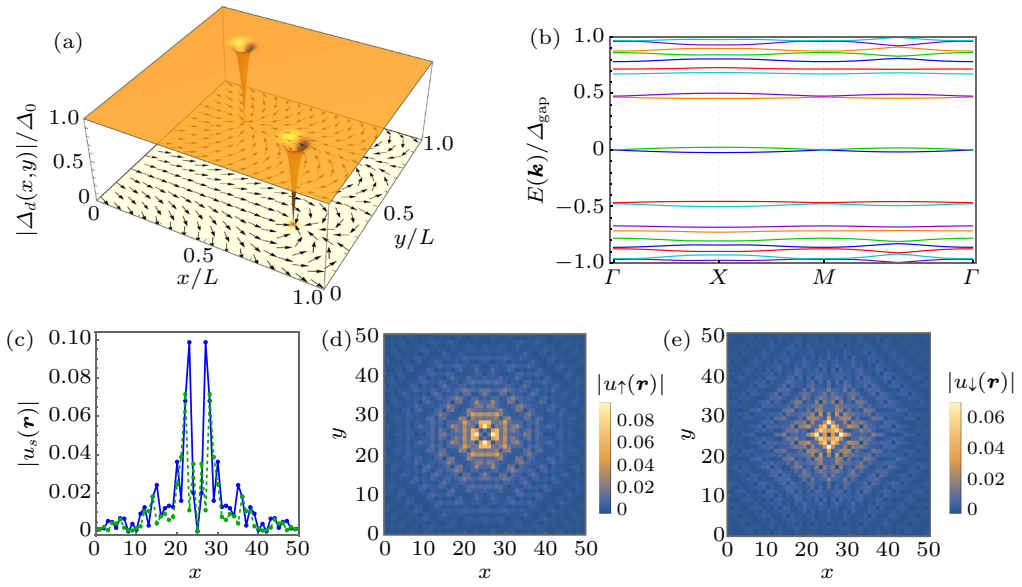


Fig. 4. (a) The magnitude and phase of the dOP $\Delta_{\rm d}(\boldsymbol{r})$ in one MUC accommodating two vortices. We set $\alpha = 10$ in Eq. (12). (b) BdG quasiparticle spectra in the magnetic BZ. $\Gamma = (0,0)$, $X = (\pi/L, 0)$, $M = (\pi/L, \pi/L)$ with MUC size $L = 60$. (c)–(e) The spatial distribution of the electron components of the zero-mode wave function around one of the two vortices. The MUC size is $L = 100$. The system parameters are the same as those in Fig. 3(b) with the associated superconducting Chern number $C_{\rm BdG} = -1$. For the hole components, we have $|v_\uparrow(\boldsymbol{r})| = |u_\uparrow(\boldsymbol{r})|$ and $|v_\downarrow(\boldsymbol{r})| = |u_\downarrow(\boldsymbol{r})|$. (c) Spin-up component of electron $|u_\uparrow(\boldsymbol{r})|$ (blue lines) and spin-up component of electron $|u_\downarrow(\boldsymbol{r})|$ (green line) for $\boldsymbol{r}$ across the vortex core along x direction. (d) and (e) Density plots of $|u_\uparrow(\boldsymbol{r})|$ and $|u_\downarrow(\boldsymbol{r})|$, respectively.

The quasiparticle energy spectrum in the magnetic BZ of the vortex lattice state is investigated, and the results are shown in Fig. 4 for a system with superconducting Chern numbers $C_{\rm BdG} = -1$. A salient feature is the emergence of two nearly dispersionless bands pinned at zero energy. We identify these flat bands as the vortex Majorana zero modes. In addition to the topologically protected zero modes, we clearly observe a series of trivial CdGM bound states within the bulk gap. Remarkably, the minigap, defined as the energy difference between the vortex MZMs and the lowest-lying CdGM states, is found to be approximately half of the bulk gap $\Delta_{\rm gap}$, as illustrated in the upper-right panel of Fig. 4. While the nearly dispersionless nature of both the MZMs and the lowest-lying CdGM states reflects their localization around the vortex center, only the MZMs are topologically pinned at zero energy due to particle-hole symmetry, whereas the lowest-lying CdGM states reside at finite energies. In the presence of weak inhomogeneities or imperfections, the MZMs remain robust due to the bulk-vortex correspondence, provided the perturbations do not close the bulk topological gap. While disorder may shift the CdGM levels, it cannot easily shift the MZMs away from zero energy without breaking particle–hole symmetry. For the pairing potential $\Delta_0 = 10$ meV in the host d-wave superconductor, we have the bulk gap $\Delta_{\rm gap} = 6$ meV seen in Fig. 2(b), and accordingly a topological minigap equals 3 meV. This large minigap is expected to provide enhanced protection of the vortex MZMs against environmental perturbations. Furthermore, the energies of the CdGM states are not equally spaced and become more closely packed near the gap edge, deviating from the expectation of the quasiclassical limit.[49] Indeed, the bulk gap $\Delta_{\rm gap} = 0.06t$ and the Fermi energy $E_{\rm F} = 0.3t$ yield a ratio $\Delta_{\rm gap}/E_{\rm F} = 0.2$, corresponding to the quantum limit.[56] We attribute this large ratio to the large pairing gap of the host d-wave superconductor and the small Fermi energy of the conduction electron as shown in Fig. 2.

The wave function of the Bogoliubov quasiparticle has four components: $u_{E,\uparrow}(\boldsymbol{r})$, $u_{E,\downarrow}(\boldsymbol{r})$, $v_{E,\uparrow}(\boldsymbol{r})$, and $v_{E,\downarrow}(\boldsymbol{r})$. The quasiparticle operator is defined as $\gamma_E^\dagger = \sum_{\boldsymbol{r},s}[u_{E,s}(\boldsymbol{r})c_{\boldsymbol{r},s}^\dagger + v_{E,s}(\boldsymbol{r})c_{\boldsymbol{r},s}]$. For zero modes, we have $u_{0,s}(\boldsymbol{r}) = v_{0,s}^*(\boldsymbol{r})$ up to a phase factor, and thus $\gamma_0^\dagger = \gamma_0$ is the Majorana operator. The MZM wave function is shown in the lower panels of Fig. 4. Our numerical results confirm that each vortex core hosts a single isolated MZM. The corresponding four components of the wave function are found to be spatially localized around the vortex centers and exhibit a characteristic oscillatory decay behavior as the distance from the core increases.

5. Conclusion

In this work, we propose a novel platform for topological superconductivity in the magnetic SkL coupled to a d-wave high-$T_{\rm c}$ superconductor. The topological properties of this hybrid system were investigated, focusing on the interplay between the SkL-induced topological band engineering and the d-wave pairing correlation. On one hand, the SkL is a magnetic texture of non-trivial topology, which generates an emergent magnetic field for conduction electrons. This emergent field manifests as an effective SOC and a quantized fictitious magnetic flux, enabling the reconstruction of normal-state electron bands and the formation of Chern bands. On the other hand, when the d-wave pairing is induced in the doped topological Hall insulator, the topological supercon-

ducting phase is realized with an odd superconducting Chern number. Beyond the obvious advantage of high T_c, the d-wave superconductor possesses a significantly larger gap amplitude than that of a conventional s-wave one. This facilitates a more robust topological gap and a sizable minigap, providing enhanced protection of the vortex MZMs in the superconducting vortex lattice state.

The experimental realization of such a heterostructure requires a delicate balance between the magnetic exchange coupling and the superconducting pairing. Sufficiently strong magnetic coupling is necessary to induce a full gap in an otherwise nodal d-wave superconductor. While a strong magnetic background from the skyrmion lattice could potentially suppress superconducting pairing, its spatially varying, noncollinear nature is generally less detrimental to d-wave correlation than that of a uniform magnetic field. Our results suggest that even in a regime of moderate coupling, the emergent topological superconductivity and MZMs can still be realized as long as the exchange field is sufficient to drive the system into a phase with an odd Chern number.

References

[1] Kitaev A 2003 *Ann. Phys.* **303** 2
[2] Nayak C, Simon S H, Stern A, Freedman M and Das Sarma S 2008 *Rev. Mod. Phys.* **80** 1083
[3] Fu L and Kane C L 2008 *Phys. Rev. Lett.* **100** 096407
[4] Xu J P, Liu C, Wang M X, Ge J, Liu Z L, Yang X, Chen Y, Liu Y, Xu Z A, Gao C L, Qian D, Zhang F C and Jia J F 2014 *Phys. Rev. Lett.* **112** 217001
[5] Liu J and Hesjedal T 2023 *Adv. Mater.* **35** 2102427
[6] Zhu Z, Zheng H and Jia J F 2021 *J. Appl. Phys.* **129** 151104
[7] Zang Y, Küster F, Zhang J, Liu D, Pal B, Deniz H, Sessi P, Gilbert M J and Parkin S S 2021 *Nano Lett.* **21** 2758
[8] Sau J D, Lutchyn R M, Tewari S and Das Sarma S 2010 *Phys. Rev. Lett.* **104** 040502
[9] Alicea J 2010 *Phys. Rev. B* **81** 125318
[10] Lutchyn R M, Sau J D and Das Sarma S 2010 *Phys. Rev. Lett.* **105** 077001
[11] Sato M and Ando Y 2017 *Rep. Prog. Phys.* **80** 076501
[12] Frolov S M, Manfra M J and Sau J D 2020 *Nat. Phys.* **16** 718
[13] Qi X L, Hughes T L and Zhang S C 2010 *Phys. Rev. B* **82** 184516
[14] Wang J, Zhou Q, Lian B and Zhang S C 2015 *Phys. Rev. B* **92** 064520
[15] Chen C Z, He J J, Xu D H and Law K T 2017 *Phys. Rev. B* **96** 041118
[16] Di Miceli D and Serra L 2023 *Sci. Rep.* **13** 19955
[17] Uday A, Lippertz G, Moors K, Legg H F, Joris R, Bliesener A, Pereira L M C, Taskin A A and Ando Y 2024 *Nat. Phys.* **20** 1589
[18] Yi H, Zhao Y F, Chan Y T, Cai J, Mei R, Wu X, Yan Z J, Zhou L J, Zhang R, Wang Z, Paolini S, Xiao R, Wang K, Richardella A R, Singleton J, Winter L E, Proksch T, Salman Z, Suter A, Balakrishnan P P, Grutter A J, Chan M H W, Samarth N, Xu X, Wu W, Liu C X and Chang C Z 2024 *Science* **383** 634
[19] Klinovaja J, Stano P, Yazdani A and Loss D 2013 *Phys. Rev. Lett.* **111** 186805
[20] Nadj-Perge S, Drozdov I K, Bernevig B A and Yazdani A 2013 *Phys. Rev. B* **88** 020407
[21] Li J, Chen H, Drozdov I K, Yazdani A, Bernevig B A and MacDonald A H 2014 *Phys. Rev. B* **90** 235433
[22] Nadj-Perge S, Drozdov I K, Li J, Chen H, Jeon S, Seo J, MacDonald A H, Bernevig B A and Yazdani A 2014 *Science* **346** 602
[23] Li J, Neupert T, Wang Z, MacDonald A H, Yazdani A and Bernevig B A 2016 *Nat. Comm.* **7** 12297
[24] Jäck B, Xie Y and Yazdani A 2021 *Nat. Rev. Phys.* **3** 541
[25] Nakosai S, Tanaka Y and Nagaosa N 2013 *Phys. Rev. B* **88** 180503
[26] Yang G, Stano P, Klinovaja J and Loss D 2016 *Phys. Rev. B* **93** 224505
[27] Rex S, Gornyi I V and Mirlin A D 2019 *Phys. Rev. B* **100** 064504
[28] Kubetzka A, Bürger J M, Wiesendanger R and von Bergmann K 2020 *Phys. Rev. Mater.* **4** 081401
[29] Bedow J, Mascot E, Posske T, Uhrig G S, Wiesendanger R, Rachel S and Morr D K 2020 *Phys. Rev. B* **102** 180504
[30] Mascot E, Bedow J, Graham M, Rachel S and Morr D K 2021 *npj Quantum Mater.* **6** 6
[31] Petrović A P, Raju M, Tee X Y, Louat A, Maggio-Aprile I, Menezes R M, Wyszyński M J, Duong N K, Reznikov M, Renner C, Milošević M V and Panagopoulos C 2021 *Phys. Rev. Lett.* **126** 117205
[32] Steffensen D, Andersen B M and Kotetes P 2021 *Phys. Rev. B* **104** 174502
[33] Steffensen D, Christensen M H, Andersen B M and Kotetes P 2022 *Phys. Rev. Res.* **4** 013225
[34] Nickel F and Heinze S 2025 *npj Spintronics* **3** 13
[35] Nagaosa N and Tokura Y 2013 *Nat. Nanotechnol.* **8** 899
[36] Mühlbauer S, Binz B, Jonietz F, Pfleiderer C, Rosch A, Neubauer A, Georgii R and Böni P 2009 *Science* **323** 915
[37] Yu X Z, Onose Y, Kanazawa N, Park J H, Han J H, Matsui Y, Nagaosa N and Tokura Y 2010 *Nature* **465** 901
[38] Heinze S, von Bergmann K, Menzel M, Brede J, Kubetzka A, Wiesendanger R, Bihlmayer G and Blügel S 2011 *Nat. Phys.* **7** 713
[39] Fert A, Reyren N and Cros V 2017 *Nature Reviews Materials* **2** 17031
[40] Khanh N D, Nakajima T, Yu X, Gao S, Shibata K, Hirschberger M, Yamasaki Y, Sagayama H, Nakao H, Peng L, Nakajima K, Takagi R, Arima T H, Tokura Y and Seki S 2020 *Nat. Nanotechnol.* **15** 444
[41] Neubauer A, Pfleiderer C, Binz B, Rosch A, Ritz R, Niklowitz P G and Böni P 2009 *Phys. Rev. Lett.* **102** 186602
[42] Kanazawa N, Onose Y, Arima T, Okuyama D, Ohoyama K, Wakimoto S, Kakurai K, Ishiwata S and Tokura Y 2011 *Phys. Rev. Lett.* **106** 156603
[43] Hamamoto K, Ezawa M and Nagaosa N 2015 *Phys. Rev. B* **92** 115417
[44] Lado J L and Fernández-Rossier J 2015 *Phys. Rev. B* **92** 115433
[45] Göbel B, Mook A, Henk J and Mertig I 2017 *New J. Phys.* **19** 063042
[46] Zhu R and Liu W 2019 *AIP Advances* **9** 115103
[47] Guan Y, Yazyev O V and Kruchkov A 2023 *Nano Lett.* **23** 4209
[48] Mandal A, Satpathy S and Nanda B R K 2025 *Phys. Rev. B* **112** 064428
[49] Caroli C, De Gennes P and Matricon J 1964 *Phys. Lett.* **9** 307
[50] Wang E, Ding H, Fedorov A V, Yao W, Li Z, Lv Y F, Zhao K, Zhang L G, Xu Z, Schneeloch J, Zhong R, Ji S H, Wang L, He K, Ma X, Gu G, Yao H, Xue Q K, Chen X and Zhou S 2013 *Nat. Phys.* **9** 621
[51] Li Z X, Chan C and Yao H 2015 *Phys. Rev. B* **91** 235143
[52] Yan Z, Song F and Wang Z 2018 *Phys. Rev. Lett.* **121** 096803
[53] Wang Q, Liu C C, Lu Y M and Zhang F 2018 *Phys. Rev. Lett.* **121** 186801
[54] Avron J E, Seiler R and Simon B 1983 *Phys. Rev. Lett.* **51** 51
[55] Campbell D J, Frachet M, Benhabib S, Gilmutdinov I, Proust C, Kurosawa T, Momono N, Oda M, Horio M, Kramer K, Chang J, Ichioka M and LeBoeuf D 2022 *Phys. Rev. Lett.* **129** 067001
[56] Hayashi N, Isoshima T, Ichioka M and Machida K 1998 *Phys. Rev. Lett.* **80** 2921